Uncovering Atomic Migrations Behind Magnetic Tunnel Junction Breakdown

Hwanhui Yun[a,b]*, Deyuan Lyu[c], Yang Lv[c], Brandon R. Zink[c], Pravin Khanal[d], Bowei Zhou[d], Wei-Gang Wang[d], Jian-Ping Wang[c]*, K. Andre Mkhoyan[a]*

[a]*Department of Chemical Engineering and Materials Science, University of Minnesota, Minneapolis, MN 55455*

[b]*Korea Research Institute of Chemical Technology, Dajeon, Korea*

[c]*Department of Electrical and Computer Engineering, University of Minnesota, Minneapolis, MN 55455*

[d]*Department of Physics, University of Arizona, Tucson, AZ 85721*

Abstract

With increasing demands for efficient data storage solutions and the advancements in computer science, spintronic magnetic tunnel junction (MTJ)-based magnetic random-access memory (MRAM) devices are promising alternatives to traditional charge-based memory devices. The applications of such spintronic devices necessitate an understanding of their ideal working principles and their breakdown mechanisms. Employing *in-situ* electrical biasing scanning transmission electron microscopy (STEM) and combining atomic-level imaging and spectroscopy, two distinct breakdown mechanisms – soft breakdown and complete breakdown – are identified and studied. At relatively low electric currents, due to electromigration, motions of the atoms in the MTJ core layers result in formation of ultra-thin regions in dielectric MgO layer separating two CoFeB ferromagnets and new edge conducting paths causing reduction of device resistance. At relatively high electric currents, combination of joule heating and electromigration results in complete breakdown of the devices by melting the layers of MTJ at considerably lower temperatures then the bulk melting points. Such real-time, atomic-level STEM study of functional nanoscale devices provides unprecedented insight into the atomistic mechanisms behind structural and compositional changes in the devices during operation, an innovative technique that can be employed to a wide variety of devices.

*Corresponding authors:

Email: yunxx133@umn.edu (H.Y.), jpwang@umn.edu (J.P.W.), mkhoyan@umn.edu (K.A.M)

Main

The rapid growth of advanced computer science, including artificial intelligence technology, large-scale problem-solving, and extensive networks, is leading to an exponential increase in both the volume of data stored and processed. This surge is fueling the demand for larger and denser data storage and transfer systems. While traditional memory devices that utilize the charge state of electrons have encountered limitations in scalability and data capacity, spintronics is leveraging the spin state of electrons in electronic devices with high speed, energy efficiency, and scalability[1-8]. Magnetic random-access memory (MRAM) unit represents a spintronic memory device with the magnetic tunnel junction (MTJ) with two resistance states.[9-11] MTJ consists of an insulating barrier layer sandwiched between two ferromagnetic (FM) layers, a reference layer (RL) and a free layer (FL), whose magnetic alignment determines the tunneling resistance through the MTJ. A parallel (P) magnetic configuration of the two layers produces the low resistance, whereas an anti-parallel (AP) configuration produces the high resistance. While the magnetic configuration can be switched through applied magnetic fields, electric fields, and currents, current-driven switching through the spin transfer-torque mechanism is more desirable and already has many applications[4,5,12,13]. Among MTJs, perpendicular MTJ (PMTJ), where FM layers have perpendicular magnetic anisotropy (PMA), offers advantages in switching currents, scalability, and thermal stability[14-16]. Nanopillar PMTJ units can be integrated into current semiconductor units, such as the complementary metal-oxide semiconductor (CMOS), and offers high scalability[17].

Insufficient understanding of the impact of the current on the PMTJ devices limits new designs and further optimization and improvements in reliability[18-20]. The failure of PMTJ devices has been linked to the ultrathin core units and nanopillar shape[21], but there is still considerable ongoing debates due to lack of direct observations. Conventional transmission electron microscopy (TEM) and analytical scanning TEM (STEM) have been successfully employed for atomic-level structural analysis of MTJ devices[22-24]. However, these TEM studies have been limited to analyses of the initial and postmortem structures of MTJ devices. Operando TEM measurements, which are capable of investigating MTJ devices in real-time operation, have not been reported. In this study, we employ *in-situ* electrical biasing STEM to investigate the atomic and chemical structures of nanoscale PMTJ under realistic operation. Nanopillar PMTJs with a Mo-capped CoFeB|MgO|CoFeB core-structure, known for its excellent perpendicular magnetic anisotropy, a large tunnel magnetoresistance ratio, and thermal tolerance[25,26], are studied here during current-driven magnetic switching. The structural changes of the core are evaluated by adopting STEM imaging and electron energy-loss spectroscopy (EELS), uncovering considerable atomic movements in the layers. Two distinct

degradation stages – soft breakdown and complete breakdown – are directly observed and linked to these atomic movements.

A schematic describing the structure of nanopillar PMTJ devices studied here is shown in Fig. 1(a). The core PMTJ unit is composed of Mo(1.2)|$Co_{20}Fe_{60}B_{20}$(1)|MgO(0.9)|$Co_{20}Fe_{60}B_{20}$(1.2-1.7)|Mo(1.9) layers and is located between bottom Ta|Ru|Ta and top Ta|Ru|Ti|Au electrodes (layer thicknesses are given in nm). The two CoFeB layers are FM layers with PMA, MgO serves as an insulating layer, and Mo acts as the buffer and capping layer. In this structure, the bottom CoFeB layer is RL and top CoFeB is FL. Details on the MTJ fabrication can be found in our previous publications[25-28]. When an electric current is applied to a PMTJ device, the tunneling resistance is measured, and the characteristic switching is observed (Fig. 1(b,c)). As expected, when the current is applied in the bottom-to-top direction (referred as '(+) biasing'), the FL becomes AP with respect to RL and P to AP switching occurs and, when the current flows in the opposite direction (referred as '(-) biasing'), AP to P switching takes place (Fig. 1(b)).

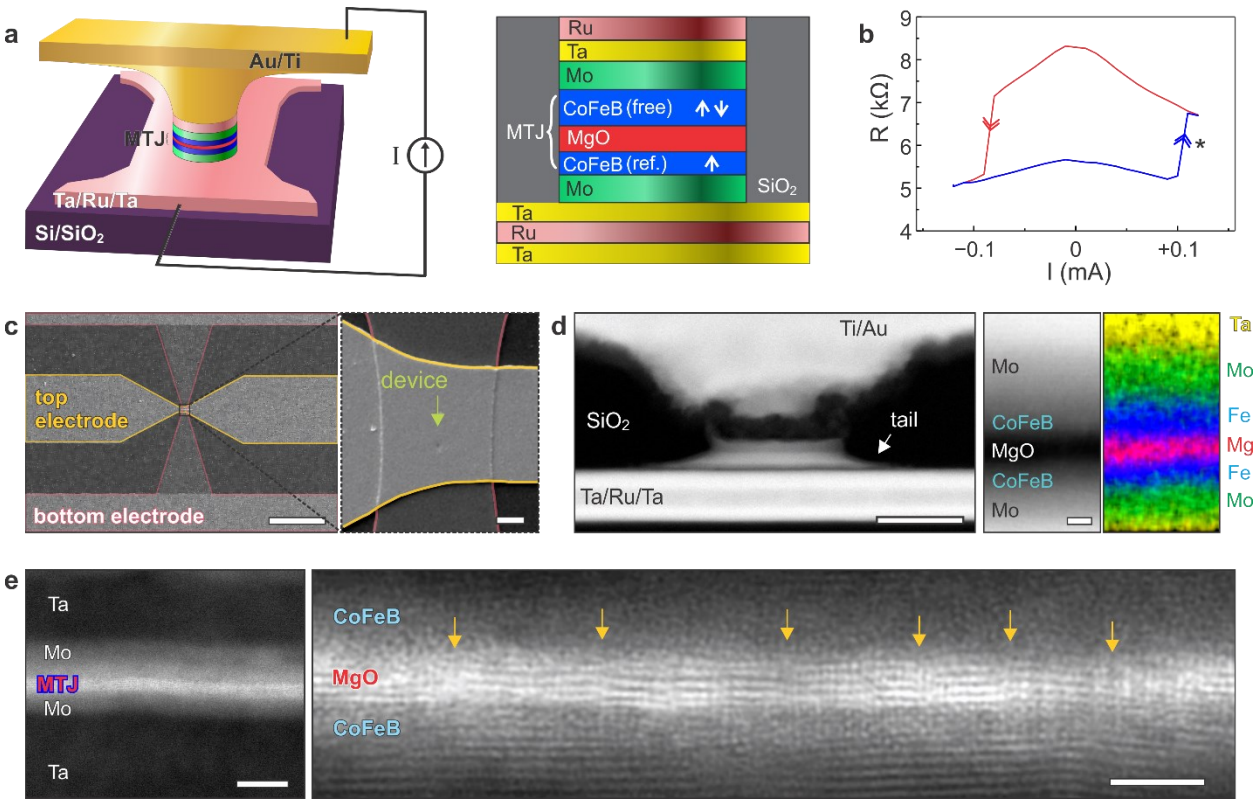

Fig. 1. Nanopillar parallel MTJ memory device with CoFeB|MgO|CoFeB core. (a) Schematics of a nanopillar PMTJ device (left) and the constituent layers (right). (b) R-I plot of a PMTJ device displaying the TMR switching with applied current, where (+) and (-) biasing directions are plotted in blue and red, respectively. The P to AP TMR switching during positive biasing is marked with an asterisk. (c) Top-down view SEM image

of a PMTJ device showing overall device with contacts with higher-magnification image showing PMTJ nanopillar in the middle. Scale bars are 50 μm and 1 μm, respectively. (d) HAADF-STEM image of a 50 nm in-diameter nanopillar PMTJ device (left) and a HAADF-STEM image with EDX elemental maps acquired from the core PMTJ unit (right). Scale bars are 50 nm and 1 nm, respectively. (e) BF-STEM images of the core PMTJ unit (left) and atomic-resolution images of the core CoFeB|MgO|CoFeB layers (right). The grain boundaries are indicated by arrows. Scale bars are 5 nm and 3 nm, correspondingly.

Structural quality of the PMTJ devices was evaluated by STEM analysis of more than 20 nanopillar PMTJ devices with a diameter of ~50 nm. A cross-sectional high-angle annular dark-field (HAADF)-STEM image of one of the PMTJ devices is shown in Fig. 1(d) (See also supplementary information (SI) Fig. S1). The nanopillars have a conical frustum shape at the base, with a diameter at the bottom Ta electrode of about ~100 nm. The 'tail' at the bottom of the PMTJ core unit is result of the standard ion milling process (see SI Fig. S2 for cases with etching or deposition failure). Additional PMTJ devices with diameter of ~200 nm were made to enhance the success rate of *in-situ* STEM sample preparation.

The atomic structures at the core MTJ units were analyzed through STEM imaging and the composition by energy dispersive X-ray (EDX) elemental maps (Fig. 1(d) and SI Fig. S1). Since the substantial atomic number difference between the core layers (MgO (Z_{MgO} = 10), CoFeB (Z_{CFB} = 22), and Mo (Z_{Mo} = 42)) and the electrodes (Ta (Z_{Ta} = 73)) makes their HAADF-STEM image analysis less reliable, bright-field (BF)-STEM was utilized to capture the lattice contrast (see SI Fig. S3 for the comparison). Such BF-STEM images of the core PMTJ unit are shown in Fig. 1(e), revealing that the MgO layer has a small grain (5 to 10 nm) polycrystalline atomic structure, rough interfaces, and a non-uniform layer thickness (d = 9 ± 2 Å) (see SI Fig. S3 for more images).

Soft breakdown

An *in-situ* STEM PMTJ devices were prepared in such a way that it allows current flow constant with the natural operation of devices. A schematic and a HAADF-STEM image of such *in-situ* STEM device are shown in Fig. 2(a) (for details of sample preparation, see SI Fig. S4). R-I curve from prepared *in-situ* device, obtained before conducting STEM measurements, shows TMR switching similar to the original device with characteristic house-like shape[29,30] (see SI Fig. S5) ruling out memristor-type resistive switching[31,32]. It should be noted here that the critical current for TMR switching is higher in the *in-situ* STEM devices due to the sample geometry, as it is thinned in STEM beam direction for the electron beam transparency.

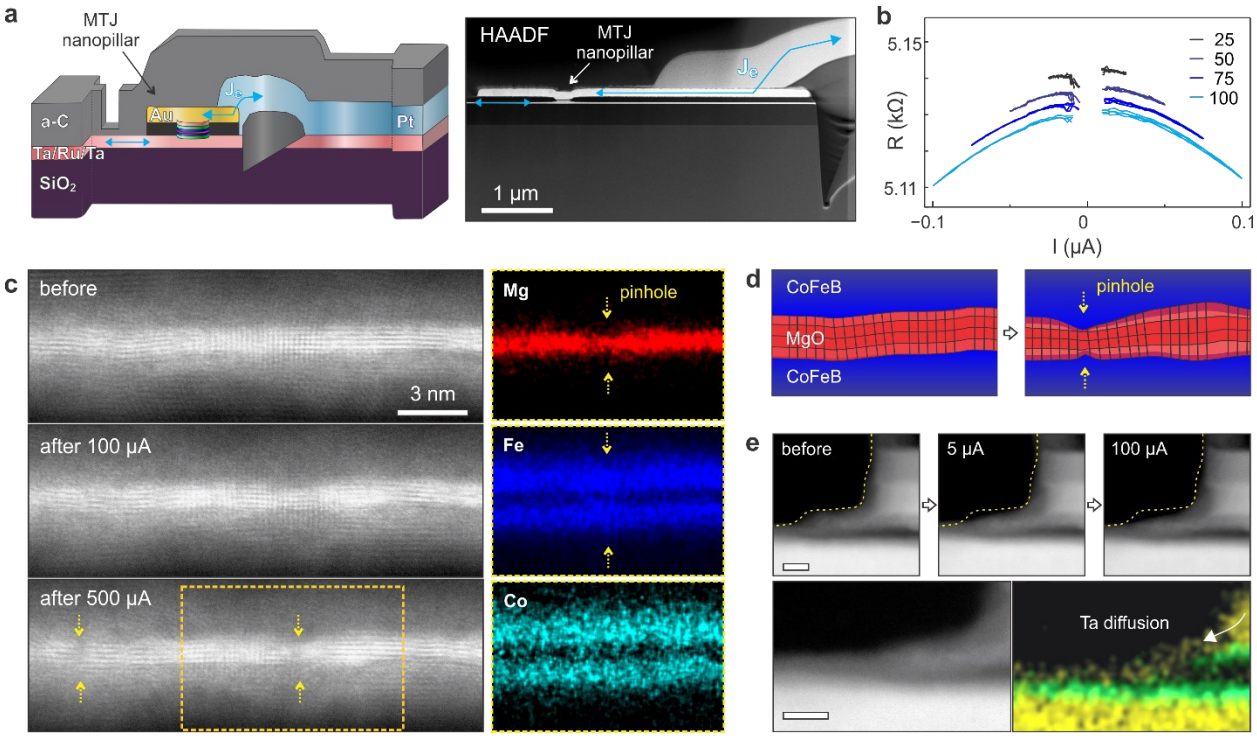

Fig. 2. Atomic-level structural changes in PMTJ causing soft breakdown of the device. (a) (left) A schematic description and (right) HAADF-STEM image of an *in-situ* STEM PMTJ device. Blue arrows indicate the current flow path. (b) A set of R-I curve obtained from *in-situ* device by applying single bias stress cycles with I_{max} from 25 μA to 100 μA. (c) A series of BF-STEM images showing the PMTJ structural modification upon biasing. Two 'pinholes' formed at 500 μA biasing are indicated by yellow arrows. EDX elemental maps, acquired from the region inside the yellow box (after 500 μA biasing), are presented on the right. (d) Schematics illustrating the formation of a pinhole in a MgO layer. (e) HAADF-STEM images showing reshaping of a nanopillar edge region during biasing. The initial (before biasing) nanopillar shape is delineated with the dashed lines. EDX elemental maps of Ta (yellow) and Mo (light green) acquired after applying bias stress cycles with the maximum current of 100 μA are presented on the bottom. Scale bars are 5 nm.

In-situ STEM experiments were conducted by running the electric bias stress cycle with a triangular pulse shape, using current as an input over time (see SI Fig. 5). To evaluate the effects of current on device performance and the structure, maximum current (I_{max}) of the triangular pulses was gradually increased, and the resistance was measured. The resistance of *in-situ* devices, obtained from the first bias stress cycle, exhibits an inversely proportional relationship with respect to STEM sample thickness (see SI Fig. 5) confirming proper current flow through the PMTJ nanopillars. Next, when a relatively small electric currents, $I_{max} \leq 500$ μA (or current density $J_{max} \leq 4 \times 10^6$ A/cm^2), are applied to *in-situ* STEM device, a gradual reduction of resistance as a function of current is observed, as shown in Fig. 2(b). Such current densities (10^6 A/cm^2) are comparable to those used in typica MTJ devices[25]. This resistance change is the indication of soft breakdown of the device. A series of STEM images of the PMTJ core were acquired after

each electric bias stress cycle and, after each cycle, a focal series of BF-STEM images were collected and, the image with the same focal depth was selected and compared with the corresponding image obtained after previous bias stress cycle (see SI Fig. S6). It should be noted that the sample damage from the beam irradiation was negligible in these STEM measurements (see SI Fig. S7). The results reveal that upon biasing the thickness of the MgO layer becomes even more non-uniform and the roughness of the interfaces with the CoFeB layers, growing from $\Delta d = 2$ Å to $\Delta d = 5$ Å, which is comparable to the original thickness of MgO layer. STEM-EDX analysis shows that Mg atoms migrate, resulting in the formation of ultra-thin MgO regions consistent with BF-STEM images (Fig. 2(c)). The ultra-thin MgO regions formed during biasing create paths for current leakage, which is a source for a soft breakdown[36-38]. It is illustrated schematically in Fig. 2(d). We believe that these thin regions in MgO are the sites referred in literatures as "pinholes". Interestingly, these pinoles do not necessarily form at the grain boundaries. They are also observed within grains, suggesting that their formation is result of the overall degradations of the MgO layer. Upon biasing, the nanopillar edge regions also show structural degradation. As shown in Fig. 2(e), the 'tail' of the top Ta layer on the PMTJ unit undergoes reshaping forming connection with the bottom Ta layer. This occurs at very low currents, even at 0.01 μA (or 80 A/cm^2), suggesting a high structural vulnerability of the nanopillar edge regions. This conducting edge path is the second critical source for leakage current contributing to the observed overall decrease of nanopillar PMTJ resistance. It should be noted that the sample damage from electron beam irradiation was negligible in these STEM measurements (see SI Fig. S7).

To further evaluate the impact of current flow on the core CoFeB|MgO|CoFeB layers, in new set of experiments, a constant current was applied to *in-situ* STEM devices first in (+) and then in (-) directions. ADF-STEM images of the exact same region of the PMTJ core were acquired before, during, and after biasing and the intensity line profiles are compared (Fig. 3(a)). The profiles before and after biasing are distinctly different from those acquired during biasing. Before and after biasing, the contrast enhancement at the Mo/Ta interface is observed (Fig. 3(a)), and the layers are distinguishable. Since the bright intensities at the Mo/Ta interface in the ADF-STEM image are absent in HAADF-STEM images (see SI Fig. S8), they are originated from the inherent strain at the interfaces. During biasing, these bright contrasts at the Mo/Ta interfaces disappear, and the boundaries between core CoFeB|MgO|CoFeB layers become smooth suggesting considerable interdiffusion between neighboring layers and strain relaxation.

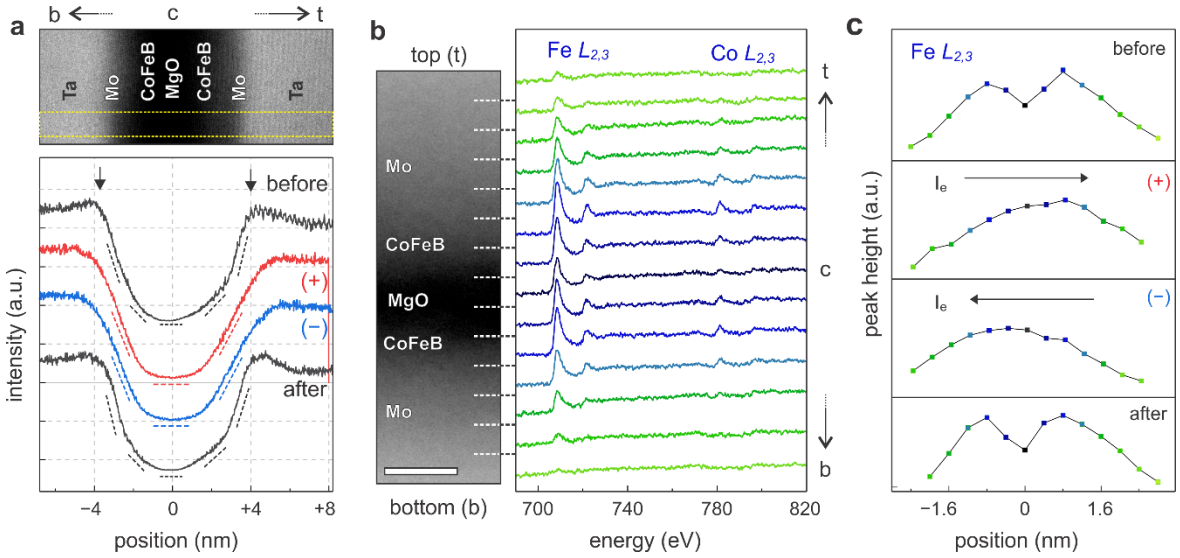

Fig. 3. Current-driven electromigration in the core layers of PMTJ devices. (a) ADF-STEM image and the intensity line profiles across a PMTJ before biasing, during biasing with applied current of +200 μA and -200 μA, and after biasing. Distinct slopes in the profiles are indicated by dashed lines. (b) EELS core-loss acquired across the PMTJ unit before biasing showing Fe $L_{2,3}$ edges and Co $L_{2,3}$ edges. STEM image of the probed core region of the PMTJ is shown on the left. Scale bar is 1 nm. (c) Peak height of the Fe $L_{2,3}$ edges under different biasing statuses. The center of the MgO layer is set as the position 0.

Core-level EELS spectra were collected from the PMTJ core unit simultaneously with the ADF-STEM images, and the results are shown in Fig. 3(b). Fe $L_{2,3}$-edges and Co $L_{2,3}$-edges measured before biasing, show peak intensities in both CoFeB layers, as expected. However, when the current is applied, distributions of Fe and Co noticeably change (Fig. 3(c) and SI Fig. S9). In the case of Fe, upon the (+) biasing, when the current flows from bottom to top, the two crests at the CoFeB layers turn to one non-symmetric broad peak centered at the top CoFeB layer. At (-) biasing, this non-symmetric broad peak is centered at the bottom CoFeB layer. The Co distribution also shows current direction-dependent intensity asymmetry, similar to the Fe case, but not very pronounced. When the current is turned off, Fe and Co intensities recover to the original profile with two crests. This directional redistribution of the elements in PMTJ core indicates electromigration-driven layer intermixing during biasing.

Migration of atoms during biasing can be primarily induced by two competing mechanisms: (i) ionic attractions to the electric field and (ii) atomic displacement by the momentum transfer from moving electrons[39]. Here Fe atoms (and to a lesser extent, Co) migrate in and out of the MgO layer upon the application of a current along the electron flow direction. The dominance of electromigration of Fe and Co by moving electron here, despite their high oxidation states (Fe^{+3} and Co^{+2}), is likely due to charge screening of migrating of Mg, O, and B (as seen in Fig. 2(c,d)). With all the observations discussed above, it can be

concluded that applying bias forces significant electromigration in PMTJ devices, which in turn, structurally and compositionally modifies the core CoFeB|MgO|CoFeB layers, triggering initial soft breakdown.

Complete breakdown

When bias stress cycles with a current, $I_{max} \approx 700$ μA (or $J_{max} \approx 6 \times 10^6$ A/cm^2), is repeatedly applied to *in-situ* STEM PMTJ device, it melts down after 45 cycles, as shown in Fig. 4(a). Upon biasing, when the current is passing through a PMTJ device, it produces joule heating, which then melts the electrodes and drives long-range (μm-scale) electromigration. Before the meltdown of a PMTJ device, even at bias stress cycles less than 30, the long-range migration of atoms is visible in Au/Ti contact. Mobile Au diffuses into Ti region and makes direct contact with the top Ru electrode (see SI Fig. S10). At this stage the R-I curve still shows TMR behavior. With repetition of bias stress cycles, the heat accumulates, top Au electrode melts, and resistance jumps up (Fig. 4(b)). At this stage, the collapse of the PMTJ core unit and the meltdown of Ta and Ru layers take place, resulting in complete breakdown of the device. EDX elemental maps acquired right after the meltdown of the PMTJ core show the top and bottom CoFeB layers merge into one, and Mg atoms of MgO layer diffuse out (Fig. 4(a)). Schematic of this complete breakdown is shown Fig. 4(c) describing the observed changes in the PMTJ. Such complete breakdown can be observed also after applying a few bias stress cycles with a higher current of $I_{max} \approx 1000$ μA (see SI Video S3 and Fig. S11). The number of cycles that it takes to achieve this breakdown is inversely proportional to the magnitude of applied current. Combination of I_{max}, number and shape of the electric bias stress cycle, and device contact area for heat dissipation determines the highest temperature the device will reach. What is observe here is co-enhancement of electromigration and joule heating in the MTJ device during its current-driven operation ultimately resulting in complete breakdown. It should be noted that this breakdown is distinctly different from the hard dielectric breakdown where abrupt decrease of resistance occurs at the critical voltage and the current flow stops[18,21,36].

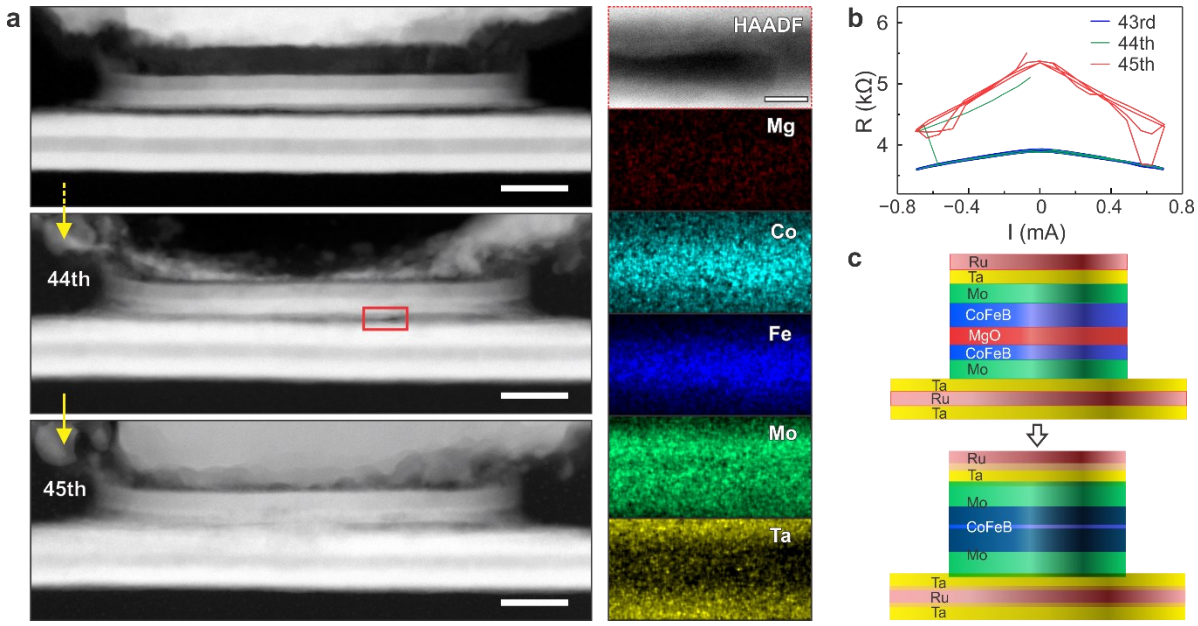

Fig. 4. Complete breakdown of PMTJ device and melting of structure. (a) HAADF-STEM images showing step-by-step the meltdown of a PMTJ device. After 45 bias stress cycles with the maximum current of 700 μA the device experiences complete destruction. Scale bars are 30 nm. EDX elemental maps from the region inside the red box are presented on the right showing dramatic intermixing of PMTJ layers. Scale bar is 3 nm. (b) Corresponding to images in (a), R-I plots upon applying bias stress cycles, where drastic increase in resistance can be seen after 44th cycle. (c) A schematic illustrating the structural meltdown of the layers in the PMTJ nanopillar.

To evaluate the effects of pure heating (without electromigration) on PMTJ devices, additional *in-situ* STEM heating experiments were conducted. In these experiments, the top Au contact melts first at ~250 °C, followed by Ru at ~450 °C, and eventually Ta at ~550 °C (see SI Fig. S12). This sequence of melting is consistent with their respective bulk melting temperatures: 1064 °C for Au, 2334 °C for Ru, and 3017°C for Ta[40]. The observed significantly lower melting temperatures in these *in-situ* STEM experiments compared to their bulk melting temperature can be attributed to the nano-sized dimensions of the layers, the ultralow vacuum level (~10^{-8} mbar) in STEM column, and the stress imposed by neighboring layers[41,42]. When biasing was applied to these samples, after completion of heating experiments, electromigration was observed again and, in some case, it showed long μm-scale migration of atoms (see SI Fig. 13). These observations confirm that upon biasing the core and electrode layers of the PMTJ device experience both considerable electromigration and joule heating. They also indicate that during operation of the device, in the presence of electromigration, the meltdown should occur at even lower temperatures than those observed in pure heating measurements.

Conclusions

In conclusion, *in-situ* electrical biasing STEM experiments performed on nanopillar PMTJ devices provided several new insights into the structural changes in the device during its breakdown. Two distinct stages and their underlying mechanisms were identified. It is observed that, at relatively small currents (≤ 500 μA), a significant electron-current-driven electromigration takes place resulting in roughening of interfaces and intermixing of core CoFeB|MgO|CoFeB layers of the PMTJ, and formation of ultra-thin regions in the MgO. In addition, a degradation of nanopillar edges is observed including a formation of nanoscale surface contacts between top and bottom Ta electrodes. These two sources of initial structural modifications of the PMTJ nanopillars are the main mechanisms of the device's soft breakdown and should be taken into consideration in new MTJ designs. At relatively high currents (> 700 μA), or high number of biasing cycles, the layers of the PMTJ melt resulting in complete breakdown of the device. Separate heating experiments point to fact that this melting of the layers occurs at much lower temperatures compared to their bulk melting point. Au contact starts to melt at temperature as low as ~250 ℃, followed by the Ru layer at ~450 ℃ inside TEM. Since at these biassing currents strong electromigration also takes place, the actual melting of the layers in the function devices might occur at even lower temperatures further emphasizing the importance of temperature increase and electromigration in new MTJ device designs.

This *in-situ* STEM study also paves the way for real-time, atomic-level investigation of other nanoscale devices, providing analysis of the structural and compositional changes that take place in the devices during their operation. The insight from such observations will be instrumental for finding ways to improve the design, quality, and reliability of these nanoscale devices.

Author contributions

H.Y. and K.A.M. conceived the project. H.Y. designed the *in-situ* electrical measurement and performed STEM experiments with input from K.A.M. D.L. and J. P. W. conceived and designed the original PMTJ device and coordinated their fabrication and electrical measurement. P.K and B.Z. fabricated the MTJ thin films with input from W.G.W. D.L. fabricated PMTJ devices. Y.L. and B.Z. assisted in the validation and interpretation of the results. H.Y. and K.A.M. prepared the manuscript with contributions from all authors.

Acknowledgements

This work was in part supported by SMART, one of seven centers of nCORE, a Semiconductor Research Corp. program, sponsored by the National Institute of Standards and Technology (NIST), the National

Science Foundation (NSF) through University of Minnesota MRSEC under Grant DMR-2011401. H.Y. would like to acknowledge the institutional research program (KK2452-20) and support program for young researchers (BSK24-131) funded by KRICT. The PMTJ device fabrication was supported in part by the Defense Advanced Research Projects Agency (DARPA) under Grant No. HR001117S0056-FP-042. Work at the University of Arizona is also supported by NSF under Grant DMR-1905783. This work was carried out at the University of Minnesota (UMN) Characterization Facility, supported in part by the NSF through the UMN MRSEC program. Portions of this work were conducted in the Minnesota Nano Center, which is supported by NSF through the National Nanotechnology Coordinated Infrastructure (NNCI) under Award No. ECCS-2025124.

Reference

[1] Hirohata, A. *et al.* Review on spintronics: Principles and device applications. *J. Magn. Magn. Mater.* **509**, 166711 (2020).

[2]Meena, J. S., Sze, S. M., Chand, U. & Tseng, T. Y. Overview of emerging nonvolatile memory technologies. *Nanoscale Res. Lett.* **9**, 526 (2014).

[3]Schenk, T., Pešić, M., Slesazeck, S., Schroeder, U. & Mikolajick, T. Memory technology—a primer for material scientists. *Rep. Prog. Phys.* **83**, 086501 (2020).

[4]Bhatti, S. *et al.* Spintronics based random access memory: a review. *Mater. Today* **20**, 530-548 (2017).

[5]Žutić, I., Fabian, J. & Das Sarma, S. Spintronics: Fundamentals and applications. *Rev. Mod. Phys.* **76**, 323-410 (2004).

[6]Wolf, S. A. *et al.* Spintronics: A spin-based electronics vision for the future. *Science* **294**, 1488-1495 (2001).

[7]Fert, A. Nobel Lecture: Origin, development, and future of spintronics. *Rev. Mod. Phys.* **80**, 1517-1530 (2008).

[8]Wang, J.-P. *et al.* A pathway to enable exponential scaling for the beyond-CMOS era in *Proceedings of the 54th Annual Design Automation Conference 2017* article 16 (Association for Computing Machinery, Austin, TX, USA, 2017).

[9]Moodera, J. S., Kinder, L. R., Wong, T. M. & Meservey, R. Large magnetoresistance at room temperature in ferromagnetic thin film tunnel junctions. *Phys. Rev. Lett.* **74**, 3273-3276 (1995).

[10]Julliere, M. Tunneling between ferromagnetic films. *Phys. Lett. A* **54**, 225-226 (1975).

[11]Butler, W. H., Zhang, X. G., Schulthess, T. C. & MacLaren, J. M. Spin-dependent tunneling conductance of Fe|MgO|Fe sandwiches. *Phys. Rev. B* **63**, 054416 (2001).

[12]Mangin, S. *et al.* Current-induced magnetization reversal in nanopillars with perpendicular anisotropy. *Nat. Mater.* **5**, 210-215 (2006).

[13]Shih, Y. C. *et al.* A reflow-capable, embedded 8Mb STT-MRAM macro with 9ns read access time in 16nm FinFET logic CMos process in *2020 IEEE International Electron Devices Meeting (IEDM).*

[14]Ikeda, S. *et al.* A perpendicular-anisotropy CoFeB–MgO magnetic tunnel junction. *Nat. Mater.* **9**, 721-724 (2010).

[15]Worledge, D. C. *et al.* Spin torque switching of perpendicular Ta|CoFeB|MgO-based magnetic tunnel junctions. *Appl. Phys. Lett.* **98**, 022501 (2011).

[16]Gajek, M. *et al.* Spin torque switching of 20 nm magnetic tunnel junctions with perpendicular anisotropy. *Appl. Phys. Lett.* **100**, 132408 (2012).

[17]Joshi, V. K., Barla, P., Bhat, S. & Kaushik, B. K. From MTJ device to hybrid CMOS/MTJ circuits: A review. *IEEE Access* **8**, 194105 (2020).

[18]Oliver, B., He, Q., Tang, X. & Nowak, J. Dielectric breakdown in magnetic tunnel junctions having an ultrathin barrier. *J. Appl. Phys.* **91**, 4348-4352 (2002).

[19]Zhao, W. S. *et al.* Failure and reliability analysis of STT-MRAM. *Microelectron. Reliab.* **52**, 1848-1852 (2012).

[20]Zhao, W. *et al.* Failure analysis in magnetic tunnel junction nanopillar with interfacial perpendicular magnetic anisotropy. *Mater.* **9**, 41 (2016).

[21]Dimitrov, D. V. *et al.* Dielectric breakdown of MgO magnetic tunnel junctions. *Appl. Phys. Lett.* **94**, 123110 (2009).

[22]Cha, J. J., Read, J. C., Buhrman, R. A. & Muller, D. A. Spatially resolved electron energy-loss spectroscopy of electron-beam grown and sputtered CoFeB⁄MgO⁄CoFeB magnetic tunnel junctions. *Appl. Phys. Lett.* **91**, 062516 (2007).

[23]Cha, J. J. *et al.* Atomic-scale spectroscopic imaging of CoFeB/Mg–B–O/CoFeB magnetic tunnel junctions. *Appl. Phys. Lett.* **95**, 032506 (2009).

[24]Xu, X. D., Mukaiyama, K., Kasai, S., Ohkubo, T. & Hono, K. Impact of boron diffusion at MgO grain boundaries on magneto-transport properties of MgO/CoFeB/W magnetic tunnel junctions. *Acta Mater.* **161**, 360-366 (2018).

[25]Lyu, D. *et al.* Sub-ns switching and cryogenic-temperature performance of Mo-based perpendicular magnetic tunnel junctions. *IEEE Electron Device Lett.* **43**, 1215-1218 (2022).

[26]Almasi, H. *et al.* Enhanced tunneling magnetoresistance and perpendicular magnetic anisotropy in Mo/CoFeB/MgO magnetic tunnel junctions. *Appl. Phys. Lett.* **106**, 182406 (2015).

[27]Almasi, H. *et al.* Effect of Mo insertion layers on the magnetoresistance and perpendicular magnetic anisotropy in Ta/CoFeB/MgO junctions. *Appl. Phys. Lett.* **109**, 032401 (2016).

[28]Newhouse-Illige, T. *et al.* Voltage-controlled interlayer coupling in perpendicularly magnetized magnetic tunnel junctions. *Nat. Commun.* **8**, 15232 (2017).

[29]Cao, K. *et al.* In-memory direct processing based on nanoscale perpendicular magnetic tunnel junctions. *Nanoscale* **10**, 21225-21230 (2018).

[30]Tezuka, N. *et al.* Perpendicular magnetic tunnel junctions with low resistance-area product: High output voltage and bias dependence of magnetoresistance. *IEEE Magnet. Lett.* **7**, 1-4 (2016).

[31]Hu, C. *et al.* The effect of oxygen vacancy on switching mechanism of ZnO resistive switching memory. *Appl. Phys. Lett.* **110**, 073501 (2017).

[32]Lyu, D. *et al.* Resistive switching behavior and mechanism of room-temperature-fabricated flexible Al/TiS_2-PVP/ITO/PET memory devices. *Curr. Appl. Phys.* **19**, 458-463 (2019).

[33]Teixeira, J. M. *et al.* Electroforming, magnetic and resistive switching in MgO-based tunnel junctions. *J. Phys. D:Appl. Phys.* **42**, 105407 (2009).

[34]Schulman, A., Paz, E., Böhnert, T., Jenkins, A. S. & Ferreira, R. Exploring multifunctionality in MgO-based magnetic tunnel junctions with coexisting magnetoresistance and memristive properties. *Adv. Funct. Mater.* **33**, 2305238 (2023).

[35]Shibata, N. *et al.* Atomic resolution electron microscopy in a magnetic field free environment. *Nat. Commun.* **10**, 2308 (2019).

[36]Oliver, B., Tuttle, G., He, Q., Tang, X. & Nowak, J. Two breakdown mechanisms in ultrathin alumina barrier magnetic tunnel junctions. *J. Appl. Phys.* **95**, 1315-1322 (2004).

[37]Wu, L. *et al.* Pinhole defect characterization and fault modeling for STT-MRAM Testing. *2019 IEEE European Test Symposium (ETS),* 1-6 (2019).

[38]Zhao, W. *et al.* Failure analysis in magnetic tunnel junction nanopillar with interfacial perpendicular magnetic anisotropy. *Mater*. (Basel) **9**, 41 (2016).

[39]Black, J. R. Electromigration—A brief survey and some recent results. *IEEE Trans. Electron Devices* **16**, 338-347 (1969).

[40]Melting points of the elements (data page) in Wikipedia. (2023, Dec. 15) https://en.wikipedia.org/wiki/Melting_points_of_the_elements_(data_page).

[41]Lai, S. L., Guo, J. Y., Petrova, V., Ramanath, G. & Allen, L. H. Size-dependent melting properties of small Tin particles: Nanocalorimetric measurements. *Phys. Rev. Lett.* **77**, 99-102 (1996).

[42]Yun, H., Zhang, D., Birol, T., Wang, J.-P. & Mkhoyan, K. A. Structural anisotropy-driven atomic mechanisms of phase transformations in the Pt–Sn System. *Nano Lett.* **23**, 7576-7583 (2023).